

Efficient Electron Transfer from Electron-Sponge Polyoxometalate to Single-Metal Site Metal–Organic Frameworks for Highly Selective Electroreduction of Carbon Dioxide

Ming-Liang Sun, Yi-Rong Wang, Wen-Wen He,* Rong-Lin Zhong, Qing-Zhi Liu, Shiyou Xu, Jing-Mei Xu, Xiao-Long Han, Xueying Ge, Shun-Li Li, Ya-Qian Lan,* Abdullah M. Al-Enizi, Ayman Nafady, and Shengqian Ma*

In this work, by combining the superiority of polyoxometalates (POMs) and catalytic single-metal site Co of metalloporphyrin, a series of mixed-valence POM-based metal-organic frameworks (MOFs) composites is synthesized by a post-modification method. The electron-transfer property of POM@PCN-222(Co) composite is significantly enhanced owing to the directional electron-transfer from POM to single-metal site Co in PCN-222(Co). In particular, H-POM@PCN-222(Co) gives a high Faradaic efficiency of 96.2% for electroreduction of CO₂ into CO and good stability over 10 h. DFT calculations confirm that the directional electron transfer, which accelerates the multi-electron transfer from the electrode to active single-metal site Co, enriches the electron density of the Co center, and ultimately reduces the energy of the rate-determining step, thus increasing the catalytic activity of CO₂ reduction reaction (CO₂RR). This work therefore suggests some new insight for the design of efficient electrocatalysts for CO₂RR.

conversion are potential methods to lower CO₂ concentration in the atmosphere.^[2–4] In contrast to CO₂ capture, CO₂ conversion is more promising, as it can convert CO₂ into low-carbon fuels or other valuable chemicals such as CO, CH₄, HCOOH, and C₂H₅OH.^[5–8] Importantly, for industrial applications, CO₂ reduction reaction (CO₂RR) is considered to be a practical and potentially valuable method for the generation of clean, renewable energy that can be undertaken even at room temperature and ambient pressure.^[9–13] Given the high thermodynamic stability, the low electron affinity of CO₂ molecules, and the competitive reaction of hydrogen evolution in the formation of the desired products, a highly selective and efficient catalyst for CO₂RR is urgently needed.^[14–21]

1. Introduction


The world's heavy reliance on fossil fuels and excessive emissions of CO₂ have led to global warming, acid rain, sea-level rise, and other serious climate problems.^[1] CO₂ storage and

In recent years, metal–organic frameworks (MOFs) composed of various transition metals ions and organic linkers have emerged in the field of electrocatalysis.^[22,23] Compared with noble metals, transition metal chalcogenides, and other catalytic materials, MOFs feature very large specific surface

M.-L. Sun, Prof. W.-W. He, Dr. J.-M. Xu
School of Chemistry and Life Science
Advanced Institute of Materials Science
Changchun University of Technology
Changchun, Jilin 130012, China
E-mail: heww@ccut.edu.cn

Y.-R. Wang, Prof. S.-L. Li, Prof. Y.-Q. Lan
School of Chemistry and Materials Science
Nanjing Normal University
Nanjing, Jiangsu 210023, China
E-mail: yqlan@njnu.edu.cn

Prof. R.-L. Zhong
Theoretical Chemistry
College of Chemistry
Jilin University
Changchun, Jilin 130023, China

 The ORCID identification number(s) for the author(s) of this article can be found under <https://doi.org/10.1002/smll.202100762>.

DOI: 10.1002/smll.202100762

Prof. Q.-Z. Liu
College of Chemistry and Pharmaceutical Sciences
Qingdao Agricultural University
Qingdao, Shandong 266109, China

Dr. S. Xu
Colgate-Palmolive Company
909 River Road, Piscataway, NJ 08855, USA

Prof. X.-L. Han
School of Chemical Engineering
Northwest University
Xi'an, Shanxi 710069, China

X. Ge, Prof. S. Ma
Department of Chemistry
University of North Texas
1508 W. Mulberry St., Denton, TX 76201, USA
E-mail: shengqian.ma@unt.edu

Dr. A. M. Al-Enizi, Prof. A. Nafady
Department of Chemistry
College of Science
King Saud University
Riyadh 11451, Saudi Arabia

area, high porosity, and consequently superior adsorptive capacity for CO₂.^[24] Additionally, the highly ordered channels, with uniformly distributed active sites, are anticipated to provide a desirable catalytic environment and affinity for CO₂ molecules.^[25] However, due to the existence of the organic components, the electrical conductivity of most MOFs is very poor, which inhibits the electron transfer to the active sites inside channels. Therefore, to improve the electrical conductivity of MOFs catalysts, researchers always mix some carbon materials such as acetylene black and carbon black Vulcan XC-72 with the catalyst crystals during electrode fabrication.^[21] However, this approach can only improve the conductivity between particles having a distance range above 100 nm. In principle, it is generally believed that electrons can hop through distances that are less than 10 Å. This made the conductivity inside MOFs as another key factor for highly efficient multiple electron transfer. In other words, electron-donating units inside the pore of MOFs materials can play a crucial role in high-efficiency electrocatalysis.

Compared with pre-assembly and in situ synthesis, post-synthetic modification method can be more promising and easily applicable for a wide range of electron-donating units.^[26–28] In this context, doping an electron-donating unit of 1,10-phenanthroline into ZIF-8 afforded a remarkable CO₂ reduction electrocatalyst.^[29] A high Faradaic efficiency for CO was accomplished through the introduction of CoCp₂ into MOF-545-Co by chemical vapor deposition.^[30] Although, the incorporation of guest molecules can greatly improve the selectivity and efficiency of CO₂RR, this multiple electron-transfer process requires more active electron-donating units thereby necessitating the search for highly active electron-transfer agents.^[31–33]

Polyoxometalates (POMs) are a family of discrete nanometric metal–oxygen clusters with novel structures comprising earth-abundant transition metals.^[34] POMs are also called electron sponges, which are rich in electron aggregates and can undergo fast, reversible, and stepwise multiple electron-transfer reactions without changing their structures.^[35] After incorporating POMs into MOFs channels, the transport distance of electrons inside MOFs can be reduced and the transport efficiency from the electrodes to the catalyst active sites can be accelerated, which is thus anticipated to increase the CO₂RR efficiency.^[14–38]

In view of the aforementioned properties, we chose MOFs and POMs based on their structural features and electrocatalytic potentials. In this respect, Co-metalloporphyrin, composed of active single-metal site Co and conjugated π -electron porphyrin flat, is conductive due to its facile electron mobility, thus, PCN-222(Co) was selected as the supporting framework.^[39–42] This MOF provides a large specific surface area not only for CO₂ molecules but also for electron-rich guest units. Furthermore, introducing the mixed-valence POM ([Co^{III}Co^{II}(H₂O)W₁₁O₃₉)⁷⁻, including one Co^{III}O₄ tetrahedra at the Keggin center and one Co^{II}O₆ octahedra at the external site)^[43] into MOF as electron-donating units will shorten the transport distance, making electron pass through more easily inside MOF pores. Hence, the interaction between the POM and the Co-metalloporphyrin-based MOF is expected to increase the catalytic activity toward CO₂RR.^[44,45]

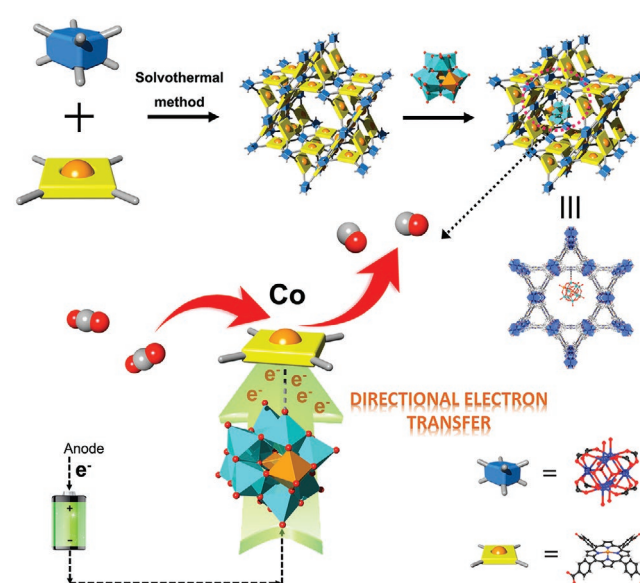
Bearing these considerations in mind, we successfully designed and synthesized a series of mixed-valence POM-based MOFs composites POM@PCN-222(M) (POM = [Co^{III}Co^{II}(H₂O)

W₁₁O₃₉]⁷⁻, M = Co, Fe, Mn, and Ni) by post-modification method. Among them, benefiting from the directional electron transfer from the POM to the single-metal site Co in PCN-222(Co) which promotes the multi-electron-transfer process, significant enhancement of electrocatalytic activity was observed for POM@PCN-222(Co). In particular, H-POM@PCN-222(Co) can selectively convert CO₂ to CO with a superior Faradaic efficiency of 96.2% and long stability exceeding 10 h. Density functional theory (DFT) calculations further confirmed this directional electron transfer, which accelerated the multi-electron transfer from the electrode to active single-metal site Co. Such behavior enriches the electron density of the Co center and ultimately decreases the energy associated with the rate-determining steps (RDSs) thus increasing the catalytic activity of CO₂RR process. The finding of this work offers a platform for designing electron-transfer channels at a molecular level, and we believe that the diverse structures of POMs will provide numerous opportunities to develop various CO₂RR catalysts.

2. Results and Discussion

2.1. Structure and Characterization of POM@PCN-222(M)

The synthetic process of POM@PCN-222(Co) composite is shown in **Scheme 1** (Taking M = Co as an example). PCN-222(Co) is isoreticular to PCN-222(Fe). The two channel sizes of PCN-222(Co) are 16 and 36 Å, respectively, which are large enough to accommodate a Keggin type POM (10 Å). Through the post-modification method, mixed-valence POM was loaded into the channels of PCN-222(Co) to afford POM@PCN-222(Co).



Scheme 1. Above: Schematic of the synthetic process and the detailed structure of POM@PCN-222(Co) composite. Below: Proposed electron-transfer scheme on the active single-metal site Co of H-POM@PCN-222(Co) for CO₂RR (Keggin type POM builds an electron-transfer channel from the electrode to active Co center and accelerates this multi-electron-transfer process to enrich the electron density of the active Co center). Blue box: Zr-based second building unit, yellow square: TCPP linker, yellow ball: Co metal center.

To study the interactions between POM molecules and different metal centers within four PCN-222(M, M = Co, Fe, Mn, and Ni) channels, the same quantity of PCN-222(Co), PCN-222(Fe), PCN-222(Mn), PCN-222(Ni) samples were immersed in POM solutions with the same concentration for 24 h (Supporting information), and the obtained samples were designated as H-POM@PCN-222(Co), H-POM@PCN-222(Fe), H-POM@PCN-222(Mn), and H-POM@PCN-222(Ni). To further study the influence of POM loading on the catalytic performance in CO₂RR, samples of POM@PCN-222(Co) containing with different amounts of POM were employed. These composites were referred to H-POM@PCN-222(Co), M-POM@PCN-222(Co), and L-POM@PCN-222(Co) (H is short for high, M is short for medium, and L is short for low).

To verify the integrity of these synthesized materials, powder X-ray diffraction (PXRD) analysis was carried out. As shown in **Figure 1a** and Figure S2, Supporting Information, the PXRD patterns of POM and PCN-222(Co) are consistent with the results reported by previous literatures, indicating the successful syntheses of these crystalline structures. The PXRD pattern of H-POM@PCN-222(Co) is similar to that of

the pristine PCN-222(Co), indicating the basic framework structure of PCN-222(Co) did not change after the formation of H-POM@PCN-222(Co). The scanning electron microscope (SEM) image shows the morphology and microstructure of the prepared samples (Figure S3, Supporting Information). The as-prepared PCN-222(Co) displays a rod-like shape with an average size of 25 μm. After loaded with POMs, the morphology of the H-POM@PCN-222(Co) remains the same as that of the pristine PCN-222(Co). The smooth surface of the rods indicates little possibility of recrystallization of POM on the PCN-222(Co) surface.

EDS line-scan data of H-POM@PCN-222(Co) are shown in Figure 1c–f. Zr Lα₁, W Mα₁, and Co Lα_{1,2} intensity lines are “single mountain” profile, indicating Zr, W, and Co contents are all inside the rod crystal. To identify the positions of POMs, the as-synthesized composite was cut by a focused ion beam (FIB) and then the FIB cross section was characterized by SEM and EDS mapping (Figure 1g–j and Figure S4, Supporting Information). The H-POM@PCN-222(Co) fiber has a hexagonal cross-section, and as expected element W of the POMs is evenly distributed inside the fiber, indicating

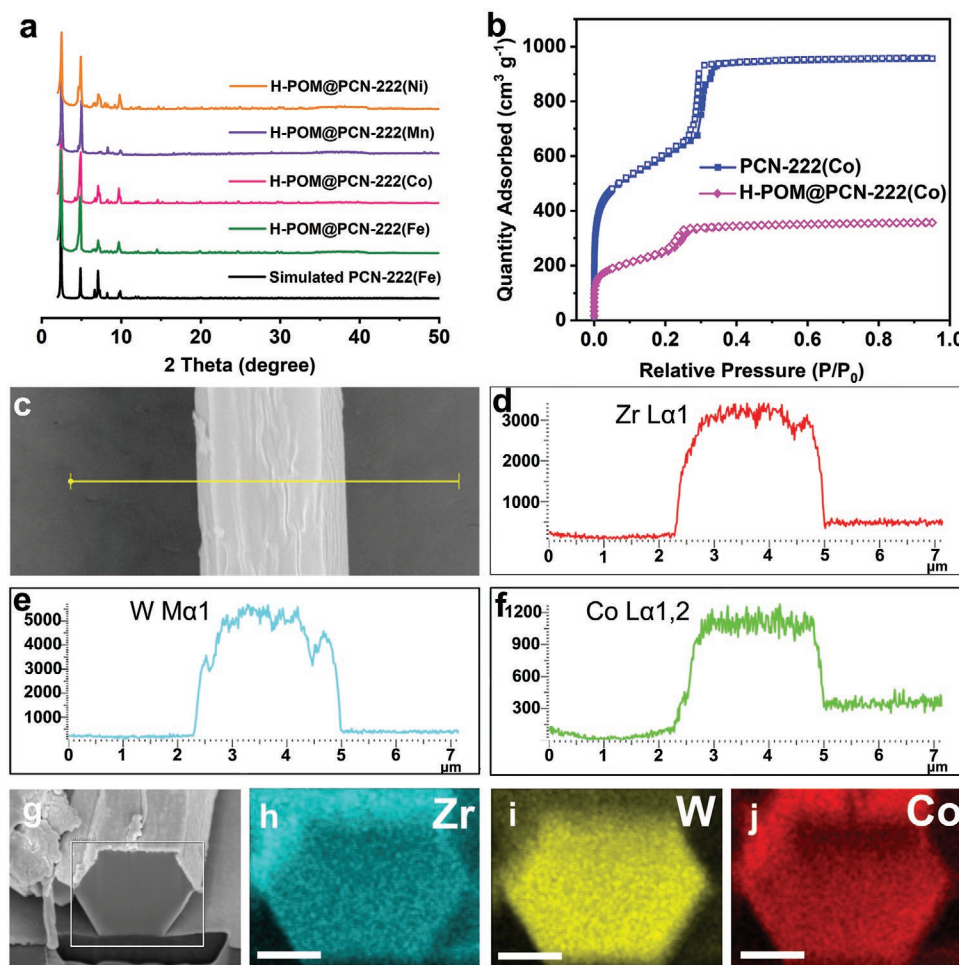


Figure 1. a) PXRD patterns of H-POM@PCN-222(Co), H-POM@PCN-222(Fe), H-POM@PCN-222(Mn), H-POM@PCN-222(Ni), and simulated PCN-222(Fe). b) N₂ adsorption isotherms of PCN-222(Co) and H-POM@PCN-222(Co). c–f) EDS line-scan of H-POM@PCN-222(Co). g) SEM image of the cross section of as-synthesized H-POM@PCN-222(Co) after the treatment by a focused ion beam. h–j) EDS mapping of the FIB cross section, indicating that POMs are encapsulated inside MOFs crystals; scale bars are 1 μm.

that POMs molecules are encapsulated within the MOF inner pores. FT-IR spectra of relevant samples are shown in Figure S5, Supporting Information.

Inductively coupled plasma optical emission spectrometry (ICP-OES) analysis was applied to estimate the loading amount of the POM in the MOF. Surprisingly, although the original concentrations of POM solutions are the same, the POM loading amounts in these four samples are different. Specifically, each unit cell in H-POM@PCN-222(Co) can accommodate about 0.57 POM, whereas much less loading amounts were found for the other three samples [0.047 for H-POM@PCN-222(Fe), 0.042 for H-POM@PCN-222(Mn), and 0.052 for H-POM@PCN-222(Ni)]. Such trend remains even at very low POM concentration (0.008 g mL⁻¹) solutions, which gave a loading amount of 0.13 POM for each unit cell for L-POM@PCN-222(Co), as summarized in Table S2, Supporting Information. These results suggest the possible strong interactions between the POM and the single-metal site Co containing porphyrin in PCN-222(Co).

Brunauer–Emmett–Teller (BET) surfaces area and pore size distributions of the samples were derived from dinitrogen adsorption measurements at 77 K (Figure 1b and Figure S6, Supporting Information). The BET surface areas of PCN-222(Co), L-POM@PCN-222(Co), M-POM@PCN-222(Co), and H-POM@PCN-222(Co) were calculated to be 2061, 1067, 920, and 822 m² g⁻¹, respectively (Table S3, Supporting Information). With the increase in the loading of POM, the BET surfaces and pore volumes of the composites decrease steadily. However, the surface area of H-POM@PCN-222(Co) is still large enough to accommodate reactants, which could directly contact with the active sites during the catalysis process.

The strong interaction between POM and the single-metal site Co of porphyrin prompted us to examine its electrocatalytic activity in CO₂RR. In doing so, the CO₂ adsorption measurements of all these POM-incorporated MOFs materials were first conducted. The CO₂ adsorption capacities are 37, 27, 24, and 20 cm³ g⁻¹ for PCN-222(Co), L-POM@PCN-222(Co), M-POM@PCN-222(Co), and H-POM@PCN-222(Co), respectively, at 298 K (Figure S7a–e, Supporting Information). It can be deduced that H-POM@PCN-222(Co) can adsorb 75 CO₂ molecules per unit cell at 1 atm and 298 K, which means the adequate supply of CO₂ molecules for electrocatalytic CO₂RR. To estimate the interactions between CO₂ molecules and the MOF framework, CO₂ adsorption isotherms at 273 and 298 K (Figure S7f, Supporting Information) were collected and the CO₂ adsorption enthalpies of the four samples were calculated using the Clausius–Clapeyron equation. Among the four samples, H-POM@PCN-222(Co) exhibited the highest CO₂ adsorption enthalpy indicating that the increase of POM loading can strengthen the interactions between CO₂ gas molecules and the MOF material, which is anticipated to facilitate the subsequent electrocatalytic reaction.

Stability is the key factor for practical application of a catalyst in CO₂RR. After soaking H-POM@PCN-222(Co) in KHCO₃ aqueous solution (0.5 M) for more than 24 h, the PXRD patterns of the H-POM@PCN-222(Co) sample remained unchanged indicative of its high chemical stability under electroreduction experiment conditions. The thermal stability of H-POM@PCN-222(Co) was assessed by thermogravimetric analysis (TGA),

which revealed that H-POM@PCN-222(Co) can be thermally stable up to 350 °C followed by the structure collapse over 350–500 °C (Figure S8, Supporting Information). Moreover, the observed different weight loss between H-POM@PCN-222(Co) and PCN-222(Co) further confirmed the loading amount of POM, which was consistent with ICP results.

2.2. The Electrocatalytic Performance of POM@PCN-222(M)

CO₂RR was performed in a two-compartment three-electrode system using CO₂-saturated 0.5 M KHCO₃ aqueous electrolytes. The catalytic performances of PCN-222(Co), PCN-222(Fe), PCN-222(Mn), and PCN-222(Ni) were first tested, and the Faradaic efficiency for CO (FE_{CO}) and FE_{H₂} were shown in the Supporting Information. The results were consistent with those reported in the literature,^[18] and linear sweep voltammetry (LSV) curves of PCN-222(Co) suggested a relatively small onset potential and a FE_{CO} value of 58.2% (Figure S9, Supporting Information).

After loading POM, the onset potential of H-POM@PCN-222(Co) was reduced to -0.35 V and the total current density was increased to 50.07 mA cm⁻² (Figure 2a). H₂ and CO were detected as the main gas products in the catalytic process through GC analysis, and no liquid products were detected by ¹H NMR spectrum (Figure S10, Supporting Information). To test the selectivity of H-POM@PCN-222(Co) for CO₂RR, we calculated the corresponding Faradaic efficiency of CO and H₂ from -0.5 to -1.0 V (Figure 2b and Figure S11a, Supporting Information). H-POM@PCN-222(Co) shows a high FE_{CO} in a wide potential range. The electrocatalytic efficiency of H-POM@PCN-222(Co) is up to 96.2% at -0.8 V, which is much higher than those of H-POM@PCN-222(Fe) (41.79%, -0.8 V), H-POM@PCN-222(Mn) (31.27%, -0.7 V), H-POM@PCN-222(Ni) (41.4%, -0.8 V), PCN-222(Co) (58.2%, -0.8 V), and POM (10.7%, -0.8 V), as well as other reported materials.^[46,47] The maxima of FE_{CO} for the six samples are shown in Figure 2c. To prove that the high electrochemical activity of H-POM@PCN-222(Co) attributes for CO₂RR, comparison tests were conducted in Ar- or CO₂-saturated KHCO₃ solution (Figure S12, Supporting Information) with much lower negative onset potential yet much larger current density observed for the test in CO₂-saturated KHCO₃ solution.

To further understand the catalytic activity of these six samples, we examined the partial current densities of CO and H₂ (Figure 2d and Figure S11b, Supporting Information) at different potentials. H-POM@PCN-222(Co) has a partial CO current density of -16.56 mA cm⁻² at -1.0 V, which was remarkably higher than H-POM@PCN-222(Fe) (-0.67 mA cm⁻², -1.0 V), H-POM@PCN-222(Mn) (-0.19 mA cm⁻², -1.0 V), and H-POM@PCN-222(Ni) (-1.1 mA cm⁻², -1.0 V), PCN-222(Co) (2.34 mA cm⁻², -1.0 V), and POM (0.53 mA cm⁻², -1.0 V). The kinetics of CO formation reaction was explained by Tafel slope (Figure 2e). Notably, the Tafel slope of H-POM@PCN-222(Co) is 216 mv·dec⁻¹, which is substantially smaller than H-POM@PCN-222(Fe) (379 mv·dec⁻¹), H-POM@PCN-222(Mn) (263 mv·dec⁻¹), H-POM@PCN-222(Ni) (422 mv·dec⁻¹), PCN-222(Co) (494 mv·dec⁻¹), and POM (234 mv·dec⁻¹). This indicates that among different H-POM@PCN-222(M) (M = Co, Mn, Ni, and Fe) systems, Co favors most the kinetics to

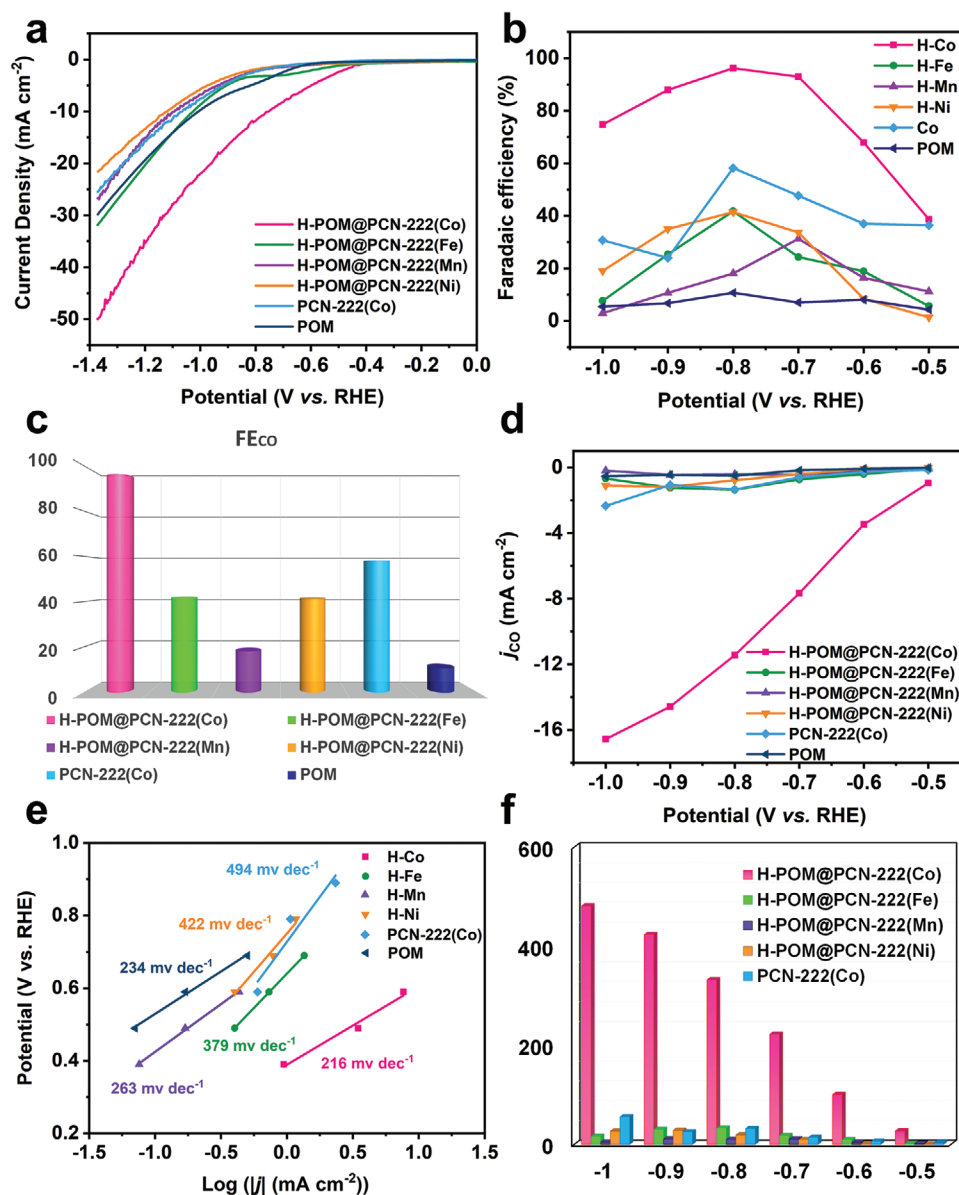


Figure 2. Electrocatalytic CO₂RR performances of H-POM@PCN-222(Co), H-POM@PCN-222(Fe), H-POM@PCN-222(Mn), H-POM@PCN-222(Ni), PCN-222(Co), and POM. a) Linear sweep voltammograms. b) Faradaic efficiencies for CO with different metals and at different potentials. c) Maximum FE_{CO} for six samples at -0.8 V (vs RHE). d) CO current density at different potentials. e) Tafel plots. f) The turnover frequency for different metals and PCN-222(Co).

generate CO. Moreover, the turnover frequency of H-POM@PCN-222(Co) is 481.4 h⁻¹ at -1.0 V, which is higher than the other three H-POM@PCN-222(M) (M = Fe, Mn, and Ni) and PCN-222(Co) (Figure 2f). The catalytic efficiency of H-POM@PCN-222(Co) also surpassed that of some reported MOF-based catalytic materials (Table S4, Supporting Information).^[20,48,49]

To further study the influence of the loading amount of the POM in electrocatalytic CO₂RR, a series of comparative samples (PCN-222[Co], L-POM@PCN-222[Co], M-POM@PCN-222[Co], and H-POM@PCN-222[Co]) were tested. Results revealed that the FE_{CO} value (96.2%) of H-POM@PCN-222(Co) was higher than the other three counterparts (PCN-222[Co] 58.2%, L-POM@PCN-222[Co] 71.2%, and M-POM@PCN-222[Co]

91.2%) (Figure S13a–c, Supporting Information). The Figure S14, Supporting Information, showed the total Faradic efficiency (CO + H₂) of H-POM@PCN-222(Co) at different potentials. Given that a new electronic channel may be established between POM and the single-metal site Co in MOF thus to improve the electron-transfer efficiency, it can be anticipated that with the increase of POM loading, the directional electron transfer will be steadily enhanced thereby promoting the CO₂RR performance gradually as observed experimentally.

The kinetics of CO formation reaction was analyzed by Tafel slope (Figure S13d, Supporting Information). Notably, the Tafel slope of H-POM@PCN-222(Co) is 216 mv·dec⁻¹, which is smaller than M-POM@PCN-222(Co) (366 mv·dec⁻¹) and

L-POM@PCN-222(Co) ($512 \text{ mv} \cdot \text{dec}^{-1}$). In this process, the load of POM further accelerates the charge transfer, improving the electrocatalytic activity.

To further explore other key factors for the excellent catalytic performance of H-POM@PCN-222(Co), the electrochemical double layer capacitance (C_{dl}) was measured to evaluate the electrochemically active surface area (ECSA) (Figure S15, Supporting Information). The C_{dl} value (9.38 mF cm^{-2}) of H-POM@PCN-222(Co) is greater than M-POM@PCN-222(Co) (9.27 mF cm^{-2}), L-POM@PCN-222(Co) (8.92 mF cm^{-2}), and PCN-222(Co) (8.86 mF cm^{-2}). The highest double capacitance of H-POM@PCN-222(Co) is an indication of the highest active electrochemical area, meaning more active sites to react with the reactants and to speed up the electrocatalytic CO_2RR process. Furthermore, electrochemical impedance spectroscopy (EIS) was undertaken to estimate the kinetics of electrode reactions. As illustrated in Nyquist plots (Figure S16, Supporting Information), the charge transfer resistance (R_{ct}) of H-POM@PCN-222(Co) (8.524Ω) is much smaller compared with PCN-222(Co) (16.38Ω), L-POM@PCN-222(Co) (13.374Ω), and M-POM@PCN-222(Co) (11.34Ω), indicating that a faster charge transfer rate can be attained when encapsulating more POM. Also, H-POM@PCN-222(Co) exhibits excellent durability of CO_2RR with almost no attenuation in the current density observed after 10 h as assessed with the chronopotentiometric curves at -0.8 V versus reversible hydrogen electrode (RHE) (Figure S17, Supporting Information). In addition, the PXRD, FT-IR spectra, and morphology of H-POM@PCN-222(Co) did not change before and after the electrocatalytic reaction (Figures S18–S20, Supporting Information). These results further demonstrate the stability of H-POM@PCN-222(Co) in electrocatalytic reactions.

To further explore the role of POM in CO_2RR and to understand the mechanism of POM@PCN-222(Co), dynamic simulations and DFT calculations were performed. As shown in Figure S21, Supporting Information, POM prefers to stay in the hexagonal channels, and adjusts itself close to the Co center of porphyrin with the Co(II) side (details of theoretical calculations are in Supporting Information). This structural tendency may do a good favor to the strong interaction between POM and active Co center resulting in a high loading amount of POM in Co containing metalloporphyrin framework. Furthermore, the distance between POM and Co center is within the range of coordination bonds, and consequently this kind of strong interaction may play a significant role in charge transfer.

The relative energy of important intermediates of the CO_2RR reactions within the part of POM-Co-TCPP (TCPP = tetra-[4-carboxyphenyl] porphyrin) has been studied. From the results of dynamic calculation, a coordination bond is found between the O of the POM and the Co of Co-TCPP in the POM@PCN-222(Co). In order to study the specific impact of the existence of POM, we simplify the MOF structure to local clusters as shown in Figure S22, Supporting Information, as the assumption that the influence of the surroundings is negligible to some extent. Thus, calculation using only one porphyrin gave a binding energy value of 0.42 eV for CO_2 to the Co center, which is within the range of Van der Waals interaction. As shown in Figure 3a, the RDS for CO_2RR of the Co-TCPP part is from $^*\text{CO}_2$ to $^*\text{COOH}$, known as a hydrogenation process,

with a free energy of 1.21 eV . When this unit received a second electron and proton, $^*\text{COOH}$ finally converted to CO molecule, which desorbs into the environment later. After incorporating POM into Co-TCPP (Figure 3b), the binding energy of CO_2 adsorption is slightly decreased to 0.32 eV , whereas the free energy of the RDS hydrogenation process is massively reduced to 0.25 eV . This conspicuous decrease in free energy can be ascribed to the continuous electron transfer from POM, as the POM is a large electron sponge and it has a dramatically good ability to trap and offer electrons.

The active site of Co-TCPP is the Co center; electrons are supplied by electrodes when there is no POM.^[40,50,51] However, the electron-transfer route is changed and a new channel is built as the POMs inside the pore can reduce the electron-transport distance and transfer electrons to the single-metal site Co through the coordination bond with Co-TCPP. The electrons of POM will eventually be supplemented by the electrode. The existence of the directional electron-transfer facilitates CO_2RR as it can deliver single-metal site Co extra electrons to convert $^*\text{CO}_2$ to $^*\text{COOH}$ more easily. This deduction is also proved by the calculation of molecular orbital as shown in Figure 3c. When the CO_2RR proceeds, the direction of electron transfer is from POM to single-metal site Co to CO_2 . These results are consistent with the experimental finding that H-POM@PCN-222(Co) has a much higher electrocatalytic FE_{CO} performance (96.2%) than that of PCN-222(Co) (58.2%). Virtually, the directional electron transfer from POM to single-metal site Co is the crucial reason for this outstanding CO_2RR performance.

Combining experimental results with the theoretical analysis above, one can draw a conclusion that incorporation of POM into PCN-222(Co) could result in the following points (Figure 3d): 1) it may bind itself to the single-metal site Co of Co-TCPP; 2) building a directional electron-transfer channel to single-metal site Co thereby accelerating this multi-electron-transfer process owing to its inherent nature as a good electron donor; and 3) enriching the electron density of the single-metal site Co and reducing the RDS energy from $^*\text{CO}_2$ to $^*\text{COOH}$, which markedly increase CO_2RR catalytic activity.

3. Conclusion

In summary, we successfully constructed a directional electron-transfer channel at a molecular level by synthesizing a series of mixed-valence POM@MOFs composites via a post-modification method. Combining the superiority of POMs and catalytic single-metal site Co in the porphyrin-based MOF, a composite with a facile electron-transfer efficiency is obtained. In this context, catalytic CO_2RR using H-POM@PCN-222(Co) was significantly promoted by the directional electron transfer from POM to single-metal site Co in PCN-222(Co), with exceptionally high Faradaic efficiency for CO of 96.2% and good stability above 10 h. DFT calculations were performed to further confirm the directional electron transfer, showing that the introduction of the POM accelerated the multi-electron transfer from the electrode to active single-metal site Co, enriched the electron density of the Co center, and ultimately reduced the RDS energy of CO_2RR catalytic process, giving rise to a high CO_2RR catalytic activity. We believe that various structures of POMs can

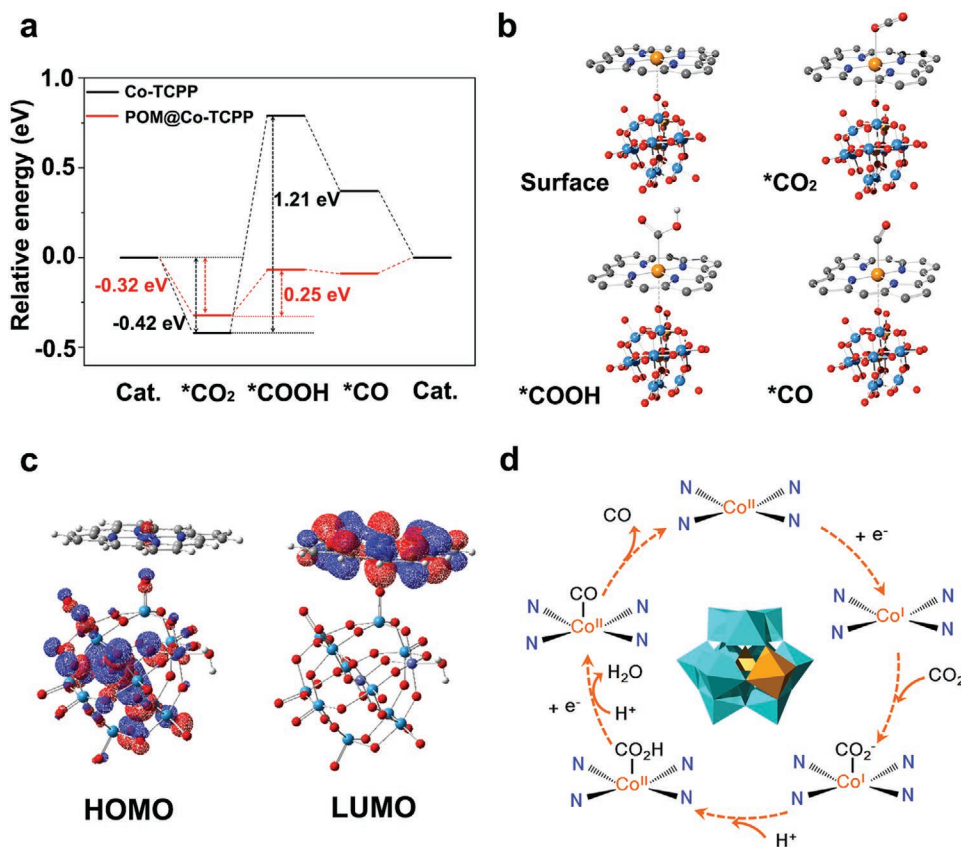


Figure 3. a) The free energy data of CO₂RR for Co-TCPP (black) and POM incorporated Co-TCPP (red). b) Steps of the CO₂RR reactions. c) HOMO and LUMO molecular orbitals. d) Mechanism of CO₂RR in H-POM@PCN-222(Co).

be implemented with other CO₂RR systems when designing high-efficiency electrocatalysts. Ultimately, this strategy is expected to open up new opportunities for designing electron-transfer channels and fabrication of highly active and selective electrocatalysts.

4. Experimental Section

Chemicals: Methyl 4-formylbenzoate was purchased from Macklin. Pyrrole, propionic acid, *N,N*-dimethylformamide (DMF), cobalt(II) chloride hexahydrate (CoCl₂·6H₂O), benzoic acid, acetone, iron(II) chloride tetrahydrate (FeCl₂·4H₂O), manganese(II) chloride tetrahydrate (MnCl₂·4H₂O), nickel(II) chloride hexahydrate (NiCl₂·6H₂O) sodium tungstate dihydrate (Na₂WO₄·2H₂O), glacial acetic acid, cobalt(II) acetate tetrahydrate (Co[OAc]₂·4H₂O), potassium persulfate (K₂S₂O₈), and thermal analysis-potassium (KNO₃) were purchased from commercial sources. 5,10,15,20-Tetrakis(4-methoxycarbonylphenyl) porphyrin (TPPCOOMe) and [5,10,15,20-Tetrakis(4-carboxyphenyl) porphyrinato]-M (M-TCPP, M = Co, Fe, Ni, Mn) were synthesized based on previous reports with modifications. All commercial chemicals were used without further purification unless otherwise mentioned.

Synthesis of K₇[Co^{III}Co^{II}(H₂O)W₁₇O₃₃]·15H₂O: POM was synthesized according to previous reports after some necessary modifications.^[43] 19.8 g (0.06 mol) of Na₂WO₄·2H₂O was dissolved in 40 mL of H₂O. Before heating to near boiling, the pH of the solution was adjusted to 7.4 by slowly adding glacial acetic acid. 13 mL of aqueous solution containing 2.5 g Co(OAc)₂·4H₂O was added drop by drop to the above system while stirring. The mixture was heated to reflux for 20 min and

then filtered while hot to remove insoluble impurities. The solution was reheated to boil for ≈10 min and 7 g of K₂S₂O₈ was slowly added several times. During the addition, a large amount of gas was generated instantaneously. After the above solution was heated to boiling, the color changed from dark green to dark brown. The mixed solution was boiled for another 10 min, then filtered while hot, and then heated to boiling. 25 mL of hot saturated KNO₃ solution was added. The mixture was cooled in an ice bath and then filtered to produce a dark brown precipitate. The filtered solids were heated and stirred in 90 °C aqueous solution for 10 min, then filtered and collected. Finally, through continuous filtration to remove impurities formed during the cooling process, a clear brown solution was obtained. After evaporation at room temperature for one week, a well-formed dark brown cubic single crystal was obtained.

Synthesis of PCN-222(Co): PCN-222(Co) was synthesized using a slightly modified method.^[42] ZrCl₄ (35 mg), Co-TCPP (25 mg), and benzoic acid (2700 mg) in 8 mL of DMF were ultrasonically dissolved in a 15 mL Pyrex vial. The mixture was heated in 120 °C oven for 48 h. After cooling down to room temperature, red needle shaped crystals were harvested by filtration. FTIR (cm⁻¹): 3420 (s), 2986 (w), 2829 (w), 1597 (s), 1560 (m), 1490 (m), 1403 (s), 1003 (s), 789 (m), 719 (m), 652 (w), and 564 (w).

Synthesis of PCN-222(Fe), PCN-222(Mn), and PCN-222(Ni): The synthesis of PCN-222(Fe), PCN-222(Mn), and PCN-222(Ni) were similar to the procedures described above except the adding of Fe-TCPP, Mn-TCPP, and Ni-TCPP.

Synthesis of L-POM@PCN-222(Co), M-POM@PCN-222(Co), H-POM@PCN-222(Co), H-POM@PCN-222(Fe), H-POM@PCN-222(Mn), and H-POM@PCN-222(Ni) (H Is Short for High Concentration, M Is Short for Middle Concentration, and L Is Short for Low Concentration): Take

the H-POM@PCN-222(Co) for example. 0.8 g of $K_7[Co^{III}Co^{II}(H_2O)W_{11}O_{39}] \cdot 15H_2O$ was dissolved in 12 mL of distilled water and 10 mL of the supernatant was taken. Then 0.02 g of PCN-222(Co) was immersed in the above-mentioned solution for 24 h. H-POM@PCN-222(Co) was collected by centrifugation and washed by deionized water several times to make sure no POM was left on the surface of the crystals. Then the sample was washed with acetone, and finally dried in vacuum at 80 °C overnight. Finally, the samples of H-POM@PCN-222(Co) were collected. Following the similar procedure, a series of composites with different POM loading were prepared. Corresponding concentration of POM solutions for preparing each complex are listed in Table S1, Supporting Information.

Characterization and Instruments: PXRD were performed on Rigaku/Smalab x-ray powder diffractometer equipped with a Cu sealed tube ($\lambda = 1.54178$) at 40 kV and 20 mA with a speed of 5° min^{-1} . The FT-IR measurements were performed on a Nicolet/iS 50 the range 4000–400 cm^{-1} . TGA was conducted on a TGA-50 (SHIMADZU) thermogravimetric analyzer heated from room temperature to 700 °C at a ramp rate of $10^\circ \text{C min}^{-1}$ under nitrogen flow of 30 mL min^{-1} . Elemental analysis was measured by ICP-OES using a POMES TJA. N_2 and CO_2 adsorption measurements were tested by Micromeritics ASAP 2020 surface area and porosity analyzer. Before gas adsorption measurements, activation processes were carried on. Fresh methanol was added and the crystals were allowed to remain for 24 h and this process was repeated twice more to remove the nonvolatile solvent. In a similar manner methylene chloride was used to remove the methanol solvent. Finally, crystals were filtered and dried overnight in a dynamic vacuum at room temperature. Before measurement, the sample was activated by degassing at 120 °C for 12 h. SEM measurements and FIB measurements were performed on a Zeiss XB 540 SEMs equipped with an Oxford energy dispersive x-ray spectroscopy.

Electrochemical Measurements: Electrocatalysis experiments of all catalysts were performed on the electrochemical workstation (Bio-Logic) in a standard three-electrode configuration in 0.5 M $KHCO_3$ (pH = 7.2). Carbon rod and Ag/AgCl were used as reference electrode and counter electrode, respectively, and modified carbon paper (1 $\text{cm} \times 2 \text{ cm}$) was used as work electrode. The electrochemical CO_2 RR performance was performed in an airtight electrochemical H-type cell, two compartments were separated by an exchange membrane (Nafion 117).

The preparation of a catalytically modified carbon paper electrode (1 $\text{cm} \times 2 \text{ cm}$) was as follows. 10 mg of an electrocatalyst and 10 mg of acetylene black were grounded and dispersed in 1 mL of a 0.5% Nafion solution and sonicated for 30 min to form a uniform catalyst ink. The ink was then dripped directly onto the carbon paper with a catalyst supporting density of $\approx 1 \text{ mg cm}^{-2}$ and dried.

The polarization curves were tested by LSV measurement with a scan rate of 5 mV s^{-1} . Polarization curves of the modified electrodes were recorded in Ar-saturated and CO_2 -saturated $KHCO_3$ solution in sequence.

The EIS measurements were made at -0.8 V (vs RHE). During the measurement process, 10 mV amplitude AC voltage was applied in the frequency range from 1000 kHz to 100 mHz. In order to estimate the ECSA, cyclic voltammograms were tested by measuring double-layer capacitance (C_{dl}) under the potential window of 0.1–0.2 V (vs Ag/AgCl) with various scan rates from 20 to 140 mV s^{-1} . In this work, all the potentials were measured versus Ag/AgCl electrode and the results were reported versus RHE based on the Nernst equation: $E \text{ (vs RHE)} = E \text{ (vs Ag/AgCl)} + 0.1989 \text{ V} + 0.059 \times \text{pH}$ (without iR compensation).

Supporting Information

Supporting Information is available from the Wiley Online Library or from the author.

Acknowledgements

M.-L.S. and Y.-R.W. contributed equally to this work. This work was financially supported by the National Natural Science Foundation

of China (Nos. 21701016 and 51803011), the Science and Technology Development Planning of Jilin Province (No. 20190103129JH), and the Education Department of Jilin Province (No. JJKH20200666KJ). This paper was also supported by the China Scholarship Council (CSC No. 201802335014). Partial support from the Robert A. Welch Foundation (B-0027) (S.M.) and Researchers Supporting Program (RSP-2021/55) at King Saud University, Riyadh, Saudi Arabia is also acknowledged.

Conflict of Interest

The authors declare no conflict of interest.

Data Availability Statement

The data that support the findings of this study are available from the corresponding author upon reasonable request.

Keywords

carbon dioxide reduction reaction, directional electron transfer, electrocatalysis, metal–organic frameworks, polyoxometalates

Received: February 5, 2021

Published online: April 4, 2021

- [1] J. D. Shakun, P. U. Clark, F. He, S. A. Marcott, A. C. Mix, Z. Liu, B. Otto-Bliesner, A. Schmittner, E. Bard, *Nature* **2012**, *484*, 49.
- [2] H. Rao, L. C. S. Schmidt, J. Bonin, M. Robert, *Nature* **2017**, *548*, 74.
- [3] P. D. Luna, R. Quintero-Bermudez, D. Cao-Thang, M. B. Ross, O. S. Bushuyev, P. Todorovic, T. Regier, S. O. Kelley, P. Yang, E. H. Sargent, *Nat. Catal.* **2018**, *1*, 103.
- [4] T. Haas, R. Krause, R. Weber, M. Demler, G. Schmid, *Nat. Catal.* **2018**, *1*, 32.
- [5] J. Wu, Y. Huang, W. Ye, Y. Li, *Adv. Sci.* **2017**, *4*, 1700194.
- [6] Y. Pan, R. Lin, Y. Chen, S. Liu, W. Zhu, X. Cao, W. Chen, K. Wu, W.-C. Cheong, Y. Wang, L. Zheng, J. Luo, Y. Lin, Y. Liu, C. Liu, J. Li, Q. Lu, X. Chen, D. Wang, Q. Peng, C. Chen, Y. Li, *J. Am. Chem. Soc.* **2018**, *140*, 4218.
- [7] Z. Miao, P. Hu, C. Nie, H. Xie, W. Fu, Q. Li, *J. Energy Chem.* **2019**, *38*, 114.
- [8] Y. Lum, J. W. Ager, *Nat. Catal.* **2019**, *2*, 86.
- [9] Q. Li, J. Fu, W. Zhu, Z. Chen, B. Shen, L. Wu, Z. Xi, T. Wang, G. Lu, J.-j. Zhu, S. Sun, *J. Am. Chem. Soc.* **2017**, *139*, 4290.
- [10] S. Gao, Y. Lin, X. Jiao, Y. Sun, Q. Luo, W. Zhang, D. Li, J. Yang, Y. Xie, *Nature* **2016**, *529*, 68.
- [11] Y. Jiao, Y. Zheng, P. Chen, M. Jaroniec, S.-Z. Qiao, *J. Am. Chem. Soc.* **2017**, *139*, 18093.
- [12] X. Duan, J. Xu, Z. Wei, J. Ma, S. Guo, S. Wang, H. Liu, S. Dou, *Adv. Mater.* **2017**, *29*, 1701784.
- [13] S. Lin, C. S. Diercks, Y.-B. Zhang, N. Kornienko, E. M. Nichols, Y. Zhao, A. R. Paris, D. Kim, P. Yang, O. M. Yaghi, C. J. Chang, *Science* **2015**, *349*, 1208.
- [14] Z. Sun, T. Ma, H. Tao, Q. Fan, B. Han, *Chem* **2017**, *3*, 560.
- [15] W. Zhu, R. Michalsky, O. Metin, H. Lv, S. Guo, C. J. Wright, X. Sun, A. A. Peterson, S. Sun, *J. Am. Chem. Soc.* **2013**, *135*, 16833.
- [16] H. Mistry, R. Reske, Z. Zeng, Z.-J. Zhao, J. Greeley, P. Strasser, B. R. Cuenya, *J. Am. Chem. Soc.* **2014**, *136*, 16473.
- [17] A. Salehi-Khojin, H.-R. M. Jhong, B. A. Rosen, W. Zhu, S. Ma, P. J. A. Kenis, R. I. Masel, *J. Phys. Chem. C* **2013**, *117*, 1627.

- [18] D. Gao, H. Zhou, J. Wang, S. Miao, F. Yang, G. Wang, J. Wang, X. Bao, *J. Am. Chem. Soc.* **2015**, *137*, 4288.
- [19] A. Klinkova, P. D. Luna, C.-T. Dinh, O. Voznyy, E. M. Larin, E. Kumacheva, E. H. Sargent, *ACS Catal.* **2016**, *6*, 8115.
- [20] Q. Lu, J. Rosen, Y. Zhou, G. S. Hutchings, Y. C. Kimmel, J. G. Chen, F. Jiao, *Nat. Commun.* **2014**, *5*, 3242.
- [21] Y.-R. Wang, Q. Huang, C.-T. He, Y. Chen, J. Liu, F.-C. Shen, Y.-Q. Lan, *Nat. Commun.* **2018**, *9*, 4466.
- [22] a) R. S. Kumar, S. S. Kumar, M. A. Kulandainathan, *Electrochem. Commun.* **2012**, *25*, 70; b) F.-L. Li, P. Wang, X. Huang, D. J. Young, H.-F. Wang, P. Braunstein, J.-P. Lang, *Angew. Chem., Int. Ed.* **2019**, *58*, 7051; c) F.-L. Li, Q. Shao, X. Huang, J.-P. Lang, *Angew. Chem., Int. Ed.* **2018**, *57*, 1888; d) J.-Y. Xue, C. Li, F.-L. Li, H.-W. Gu, P. Braunstein, J.-P. Lang, *Nanoscale* **2020**, *12*, 4816.
- [23] O. M. Yaghi, H. L. Li, *J. Am. Chem. Soc.* **1995**, *117*, 10401.
- [24] G. Paille, M. Gomez-Mingot, C. Roch-Marchal, B. Lassalle-Kaiser, P. Mialane, M. Fontecave, C. Mellot-Draznieks, A. Dolbecq, *J. Am. Chem. Soc.* **2018**, *140*, 3613.
- [25] H.-C. Zhou, J. R. Long, O. M. Yaghi, *Chem. Rev.* **2012**, *112*, 673.
- [26] C. Wang, D. Liu, W. Lin, *J. Am. Chem. Soc.* **2013**, *135*, 13222.
- [27] S. M. Cohen, *Chem. Sci.* **2010**, *1*, 32.
- [28] T. Zhou, Y. Du, A. Borgna, J. Hong, Y. Wang, J. Han, W. Zhang, R. Xu, *Energy Environ. Sci.* **2013**, *6*, 3229.
- [29] a) S. Dou, J. Song, S. Xi, Y. Du, J. Wang, Z.-F. Huang, Z. J. Xu, X. Wang, *Angew. Chem., Int. Ed.* **2019**, *58*, 4041; b) S. Dou, J. Song, S. Xi, Y. Du, J. Wang, Z.-F. Huang, Z. J. Xu, X. Wang, *Angew. Chem.* **2019**, *131*, 4081.
- [30] Z. Xin, Y.-R. Wang, Y. Chen, W.-L. Li, L.-Z. Dong, Y.-Q. Lan, *Nano Energy* **2020**, *67*, 104233.
- [31] A. Aijaz, A. Karkamkar, Y. J. Choi, N. Tsumori, E. Roennebro, T. Autrey, H. Shioyama, Q. Xu, *J. Am. Chem. Soc.* **2012**, *134*, 13926.
- [32] J. J. Walsh, A. M. Bond, R. J. Forster, T. E. Keyes, *Coord. Chem. Rev.* **2016**, *306*, 217.
- [33] a) H. G. T. Ly, G. Absillis, R. Janssens, P. Proost, T. N. Parac-Vogt, *Angew. Chem., Int. Ed.* **2015**, *54*, 7391; b) H. G. T. Ly, G. Absillis, R. Janssens, P. Proost, T. N. Parac-Vogt, *Angew. Chem.* **2015**, *127*, 7499.
- [34] H. N. Miras, J. Yan, D.-L. Long, L. Cronin, *Chem. Soc. Rev.* **2012**, *41*, 7403.
- [35] A. Proust, B. Matt, R. Villanneau, G. Guillemot, P. Gouzerh, G. Izzet, *Chem. Soc. Rev.* **2012**, *41*, 7605.
- [36] a) N. Li, J. Liu, B.-X. Dong, Y.-Q. Lan, *Angew. Chem., Int. Ed.* **2020**, *59*, 20779; b) N. Li, J. Liu, B.-X. Dong, Y.-Q. Lan, *Angew. Chem.* **2020**, *132*, 20963.
- [37] M. Zhang, A. M. Zhang, X.-X. Wang, Q. Huang, X. Zhu, X.-L. Wang, L.-Z. Dong, S.-L. Li, Y.-Q. Lan, *J. Mater. Chem. A* **2018**, *6*, 8735.
- [38] a) S. Mukhopadhyay, J. Debgupta, C. Singh, A. Kar, S. K. Das, *Angew. Chem., Int. Ed.* **2018**, *57*, 1918; b) S. Mukhopadhyay, J. Debgupta, C. Singh, A. Kar, S. K. Das, *Angew. Chem.* **2018**, *130*, 1936.
- [39] K. Leung, I. M. B. Nielsen, N. Sai, C. Medforth, J. A. Shelnutt, *J. Phys. Chem. A* **2010**, *114*, 10174.
- [40] D. Behar, T. Dhanasekaran, P. Neta, C. M. Hosten, D. Ejeh, P. Hambright, E. Fujita, *J. Phys. Chem. A* **1998**, *102*, 2870.
- [41] G. Ramirez, M. Lucero, A. Riquelme, M. Villagran, J. Costamagna, E. Trollund, M. J. Aguirre, *J. Coord. Chem.* **2004**, *57*, 249.
- [42] a) D. Feng, Z.-Y. Gu, J.-R. Li, H.-L. Jiang, Z. Wei, H.-C. Zhou, *Angew. Chem., Int. Ed.* **2012**, *51*, 10307; b) D. Feng, Z.-Y. Gu, J.-R. Li, H.-L. Jiang, Z. Wei, H.-C. Zhou, *Angew. Chem.* **2012**, *124*, 10453.
- [43] F. Song, Y. Ding, B. Ma, C. Wang, Q. Wang, X. Du, S. Fua, J. Song, *Energy Environ. Sci.* **2013**, *6*, 1170.
- [44] N. Kornienko, Y. Zhao, C. S. Kiley, C. Zhu, D. Kim, S. Lin, C. J. Chang, O. M. Yaghi, P. Yang, *J. Am. Chem. Soc.* **2015**, *137*, 14129.
- [45] D. Feng, W.-C. Chung, Z. Wei, Z.-Y. Gu, H.-L. Jiang, Y.-P. Chen, D. J. Darensbourg, H.-C. Zhou, *J. Am. Chem. Soc.* **2013**, *135*, 17105.
- [46] X. Li, W. Bi, M. Chen, Y. Sun, H. Ju, W. Yan, J. Zhu, X. Wu, W. Chu, C. Wu, Y. Xie, *J. Am. Chem. Soc.* **2017**, *139*, 14889.
- [47] R. Haldar, K. Batra, S. M. Marschner, A. B. Kuc, S. Zahn, R. A. Fischer, S. Braese, T. Heine, C. Woell, *Chem. - Eur. J.* **2019**, *25*, 7847.
- [48] H. Idan, D. S. Matthew, D. Pravas, P. K. Clifford, K. F. Omar, T. H. Joseph, *ACS Catal.* **2015**, *5*, 6302.
- [49] C. E. Tornow, M. R. Thorson, S. Ma, A. A. Gewirth, P. J. A. Kenis, *J. Am. Chem. Soc.* **2012**, *134*, 19520.
- [50] C. Costentin, S. Drouet, M. Robert, J.-M. Saveant, *J. Am. Chem. Soc.* **2012**, *134*, 19949.
- [51] M. Garcia, M. J. Aguirre, G. Canzi, C. P. Kubiak, M. Ohlbaum, M. Isaacs, *Electrochim. Acta* **2014**, *115*, 146.